Cell Reports

Resource

Region-resolved multi-omics of the mouse eye

Graphical abstract

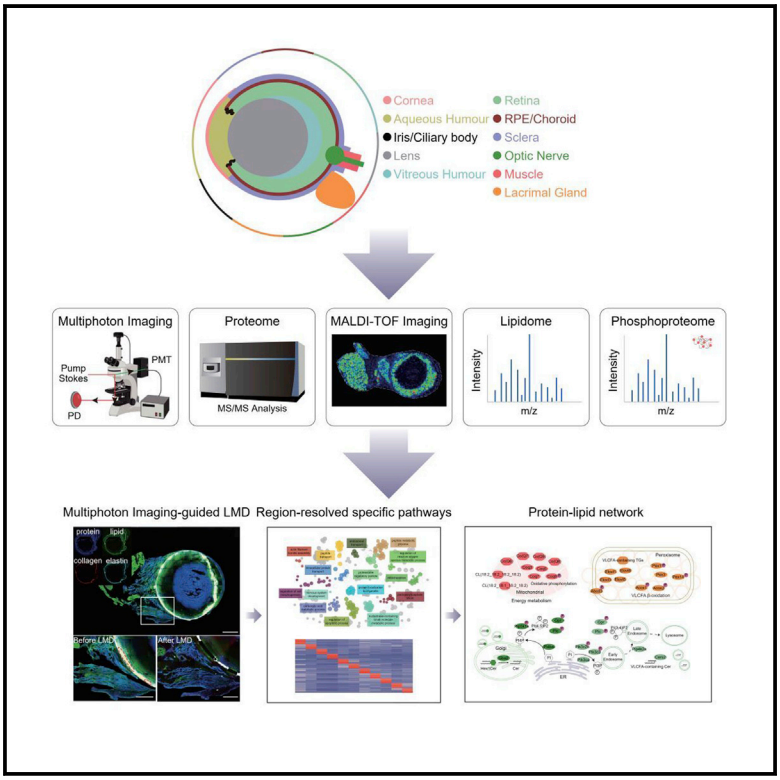

Highlights

- Region-resolved multi-omics deciphers the complex molecular features of the mouse eye
- Multiphoton imaging provides aerial view of the distribution of molecules
- Proteomics analysis reveals the distinguished pathways functioning in each region
- Region-specific protein-lipid connections are identified in the four mouse eye regions

Authors

Hang Xiang, Bohan Zhang, Yunzhi Wang, ..., Rongkui Luo, Minbiao Ji, Chen Ding

Correspondence

minbiaoj@163.com (M.J.), chend@fudan.edu.cn (C.D.)

In brief

The eye is a complex organ, which consists of multiple compartments with unique and specialized properties that reflect their varied functions. Xiang et al. present a region-resolved mouse eye proteome and lipidome that provides a physiological reference map that may serve as a resource for the public in the future.

Xiang et al., 2023, Cell Reports *42*, 112121
February 28, 2023
https://doi.org/10.1016/j.celrep.2023.112121

CellPress

Cell Reports

CellPress
OPEN ACCESS

Resource

Region-resolved multi-omics of the mouse eye

Hang Xiang,[1] Bohan Zhang,[2] Yunzhi Wang,[1] Ning Xu,[1] Fan Zhang,[1] Rongkui Luo,[3] Minbiao Ji,[2,*] and Chen Ding[1,4,*]

[1]State Key Laboratory of Genetic Engineering and Collaborative Innovation Center for Genetics and Development, School of Life Sciences, Institute of Biomedical Sciences, Human Phenome Institute, Zhongshan Hospital, Fudan University, Shanghai 200433, China

[2]State Key Laboratory of Surface Physics and Department of Physics, Human Phenome Institute, Multiscale Research Institute of Complex Systems, Academy for Engineering and Technology, Key Laboratory of Micro and Nano Photonic Structures (Ministry of Education), Fudan University, Shanghai 200433, China

[3]Department of Pathology, Zhongshan Hospital Fudan University, Shanghai, China

[4]Lead contact

*Correspondence: minbiaoj@163.com (M.J.), chend@fudan.edu.cn (C.D.)

https://doi.org/10.1016/j.celrep.2023.112121

SUMMARY

The eye is a complex organ consisting of multiple compartments with unique and specialized properties, and small disturbances in one eye region can result in impaired vision and blindness. Although there have been advancements in ocular research, the hierarchical molecular network in region-wide resolution, indicating the division of labor and crosstalk among different eye regions, is not yet comprehensively illuminated. Here, we present an atlas of region-resolved proteome and lipidome of mouse eye. Multiphoton microscopy-guided laser microdissection combined with in-depth label-free proteomics identifies 13,536 proteins across various mouse eye regions. Further integrative analysis of spectral imaging, label-free proteome, and imaging mass spectrometry of the lipidome and phosphoproteome reveals distinctive molecular features, including proteins and lipids of various anatomical mouse eye regions. These deposited datasets and our open proteome server integrating all information provide a valuable resource for future functional and mechanistic studies of mouse eye and ocular disease.

INTRODUCTION

The eye is a complex organ. At the anatomical level, it is composed of the tear film, conjunctiva, cornea, aqueous humor, iris, ciliary body, lens, vitreous humor, retina, choroid, sclera, and optic nerve. The ocular adnexa consist of the lacrimal apparatus, eyelids, extraocular muscles, and orbit. A clear vision needs all the eye elements to function well together. Small disturbances in one eye region can result in impaired vision and blindness. By 2020, an estimated 596 million people worldwide had distance vision impairment, and an estimated 43.3 million people were blind.[1] The most common causes of vision impairment in adults are uncorrected refractive error, cataract, glaucoma, age-related macular degeneration (AMD), diabetic retinopathy, corneal scarring, and trachoma.[2] However, the study about protein composition in dissimilar regions of the mouse eye is relatively incomplete.

Previous studies have focused on defining differences between specific regions of the eye or single-diseased eye compartments. One eye disease usually associates with or affects multiple eye regions. For example, AMD is a disease that affects the macular region of the retina, causing progressive loss of central vision. Early-stage AMD includes clinical signs such as drusen and abnormalities of the retinal pigment epithelium (RPE). Late-stage AMD can be neovascular or non-neovascular. Studies have reported that tear film and aqueous humor proteome in AMD can provide new insights into the pathogenesis and potential biomarkers.[3,4] The revelation of molecular characteristics of the mouse eye at the anatomical level, particularly the healthy-state mouse eye, would be an important starting point to investigate ocular disease.

Recent advances in mass spectrometry (MS)-based omics technology now allow very deep identification. Here, we set out to generate the spatial multi-omics of the mouse eye across 11 anatomical regions through the combination of multiphoton imaging, laser microdissection (LMD), MS-based proteomics and lipidomics, and MALDI-TOF imaging. We employed the multiphoton imaging-guided LMD, which to a great extent conserved the spatial and original context of tissues. Also, the multiphoton imaging provided an aerial view of the distribution of proteins and lipids across the whole mouse eye regions, giving us better knowledge on how to handle the proteome and lipidome data. For in-depth mapping of the mouse eye proteome, high-sensitivity sample preparation, peptide fractionation, and an advanced label-free liquid chromatography-tandem MS (LC-MS/MS) workflow coupled to an Orbitrap Fusion Lumos were performed to quantify a total of more than 13,000 proteins at the region-resolved level, which tremendously replenished the mouse eye proteome database. Lipidome-based MALDI-TOF/TOF imaging and MS/MS analysis revealed the distinguished and significant lipid classes that contributed in each region and also region-specific protein-lipid connections combined with our proteomic data. To verify our findings of region-specific proteins and protein-lipid connections, we further conducted the

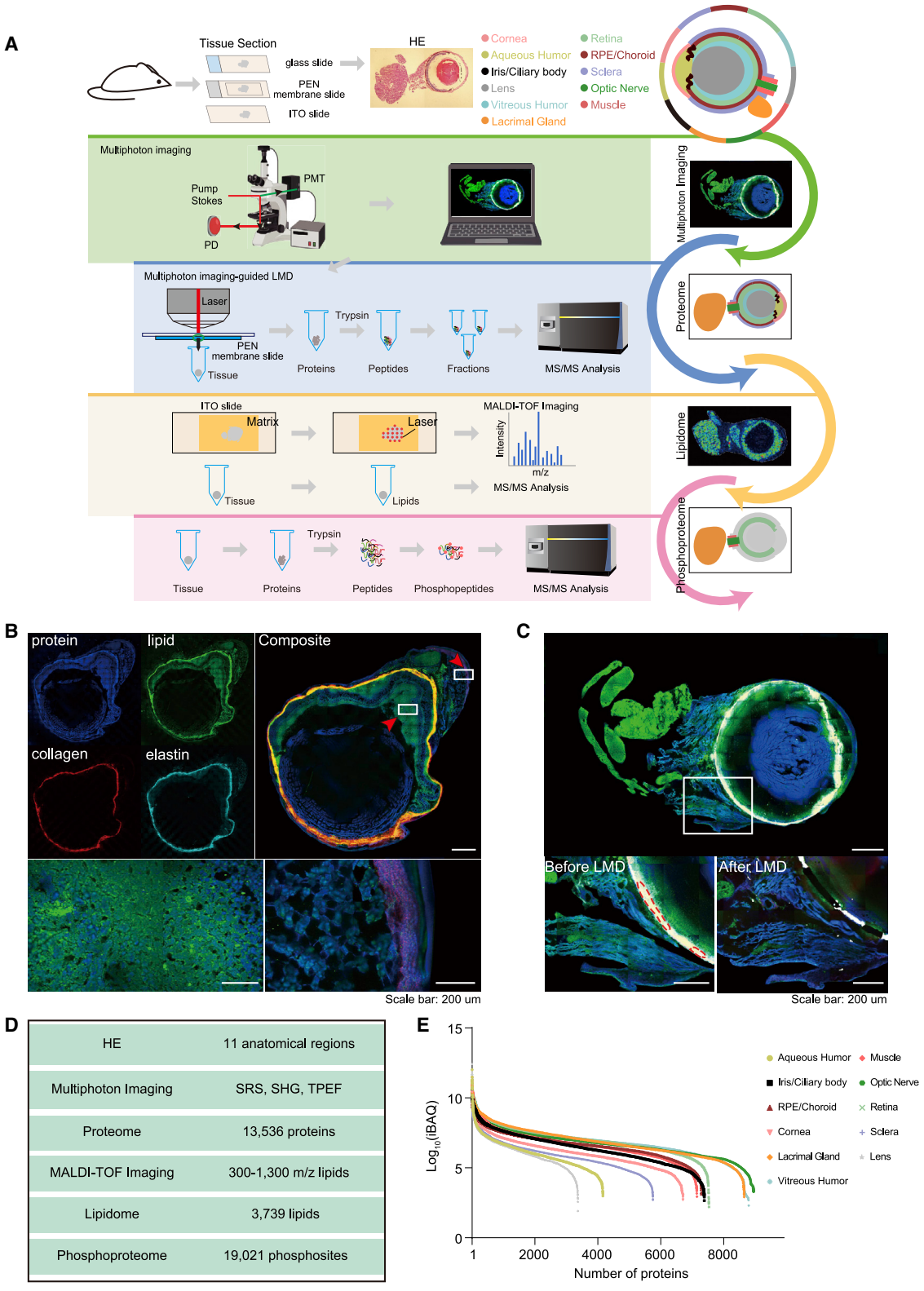

HE	11 anatomical regions
Multiphoton Imaging	SRS, SHG, TPEF
Proteome	13,536 proteins
MALDI-TOF Imaging	300-1,300 m/z lipids
Lipidome	3,739 lipids
Phosphoproteome	19,021 phosphosites

Figure 1. Region-resolved multi-omics of the mouse eye

(A) The workflow of the sample collection for H&E staining, multiphoton imaging, proteome, and MALDI-TOF imaging.

(B) Multiphoton imaging of the mouse eye, including protein, lipid, collagen, and elastin channels.

(legend continued on next page)

immunohistochemistry (IHC) staining of region-specific proteins and collected the phosphoproteomic data of mouse eye regions. Our datasets and open proteome server (http://www.eye.mouseprotein.cn) could serve as a rich resource for the eye health research community to investigate the molecular basis for region-specific functions.

RESULT

Workflow design of multiphoton imaging-guided LMD

We obtained 11 histological regions from C57/BL6 mice, including cornea, aqueous humor, iris/ciliary body, lens, vitreous humor, retina, RPE/choroid, sclera, optic nerve, eye muscle, and lacrimal gland (Figure 1A). Due to the liquid state and the small size of mouse eye, aqueous humor and vitreous humor were collected by dissection and centrifugation (STAR methods). Other regions were obtained through multiphoton imaging-guided LMD precisely (Figures 1B, 1C, and S1A–S1C; STAR methods).

Our imaging system used multimodal multiphoton microscopy, including stimulated Raman scattering (SRS), second-harmonic generation (SHG), and two-photon excited fluorescence (TPEF) imaging modalities to detect the distribution of lipids and protein, collagen, and elastin[5,6] (Figure 1D). The schematic energy diagrams are shown in Figure S1A. As a label-free and sensitive imaging modality, multimode microscopy allows mapping of molecular species in sections or fresh tissues with high imaging speed.[7] In our work, each field of view was imaged with 1s to quickly yield the overall chemical maps of the tissue, which helped identify different anatomical regions. When the region of interest (ROI) was decided, the laser power was then increased (240 mW post-objective) and scanned along the defined dissection border on polyethylene naphthalate (PEN) membrane slide (Figure S1B), and the condenser was switched to centrifuge to collect tissue, as shown in Figure S1C. Anatomical regions and region-specific structures in the mouse eye could be clearly distinguished by the distributions of protein, lipid, collagen, and elastin. Retina, RPE/choroid, optic nerve, muscle, and lacrimal gland were possessed with the high expression of lipid, and RPE/choroid also showed a strong expression level of collagen and elastin (Figure 1B).

A region-resolved proteomic map of the mouse eye

For in-depth mapping of the mouse eye proteome, LC-MS/MS was performed on the Easy-nLC liquid chromatography system coupled to an Orbitrap Fusion Lumos Tribrid platform with field asymmetric ion mobility spectrometry (FAIMS) (Figure 1A). At least three biological repeats were performed in each region. A principal-component analysis (PCA) was used to visualize variation and to highlight robust patterns in the datasets in a two-dimensional score plot (Figure S1D). The biological replicates clearly clustered together, demonstrating excellent technical and biological reproducibility. A total of 13,536 proteins were called at 1% false discovery rate (FDR) at three levels: peptide-spectrum match (PSM), peptide, and protein group level (FDR) (Figure 1D). We identified 8,948 proteins in the optic nerve, 8,792 proteins in vitreous humor, 8,650 proteins in lacrimal gland, 7,529 proteins in retina, 7,380 proteins in iris/ciliary body, 7,287 proteins in RPE/choroid, 7,145 proteins in eye muscle, 6,705 proteins in cornea, 5,747 proteins in sclera, 4,160 proteins in aqueous humor, and 3,365 proteins in lens (Figure S1E; Table S1). The protein abundance was first calculated by intensity-based absolute quantification (iBAQ), then normalized as fraction of total (FOT), allowing for comparison among different experiments. In addition, the reference proteome is highly dynamic, spanning about seven orders of magnitude measured by the protein abundances (iBAQ) (Figure 1E).

To further verify the accuracy of our data, we compared our data with reported eye proteome datasets.[8,9] As a result, our proteome data identified 13,536 proteins in the whole mouse eye, covering 9,589 proteins (85.7%) identified in the study "Mass spectrometry-based draft of the mouse proteome"[8] (Figure S2A). At the region-resolved level, our data covered 65.1%–85.4% of proteins in each eye region reported in the study "The Human Eye Proteome Project"[9] (Figure S2B). Moreover, we identified more than 2,000 different proteins in aqueous humor, vitreous humor, iris/ciliary body, and RPE/choroid compared with reported studies[9–13] (Figure S2B). Our data obtained deep coverage of the mouse eye proteome and tremendously replenished the mouse eye proteome database, which could serve as a rich resource for eye research in the future.

We calculated the median and maximum FOT values in all tissues where they were detected and used them to perform a density plot analysis of the protein expression patterns across the 11 regions. This analysis stratified the proteins into three categories: non-ubiquitous proteins (6,722 proteins), which were highly expressed in only a few regions with a transformed median expression value <0.5; and ubiquitous proteins (2,491 proteins), which were expressed in a wide variety of regions with a transformed median expression value >0.5; among them, the expression of 223 proteins, such as Agpat3, Glud1, Ap2b1, Atp6v0a1, and Atp6v1a, which exhibited a maximum value of less than 10 times the median value, were defined as ubiquitous-uniform proteins (Figure 2A; Table S2). Consistent with their wide distribution, the ubiquitous-uniform proteins mainly function in biological functions, including metabolic process, localization, transport, nervous system development, among others (Figure 2C).

Transcription factors (TFs) drive various biological processes ranging from embryonic development to carcinogenesis. In the proteome data, a total of 342 TFs were detected, ranging from 20 TFs in aqueous humor to 177 TFs in the lacrimal gland (Figure 2B; Table S2). We determined which TFs are region specific based on the criterion that the expression level of a TF in a certain region was found to be two times greater than the average of the expression levels in all regions. Considerable region-specific TFs were identified in the lacrimal gland, optic nerve, and retina, whereas a smaller number of region-specific TFs were identified in the lens and aqueous humor (Figure 2B). To this end, we

(C) Multiphoton imaging-guided laser microdissection.
(D) Summary of the data and metadata generated in this study.
(E) Dynamic range of 11 regions in the mouse eye.

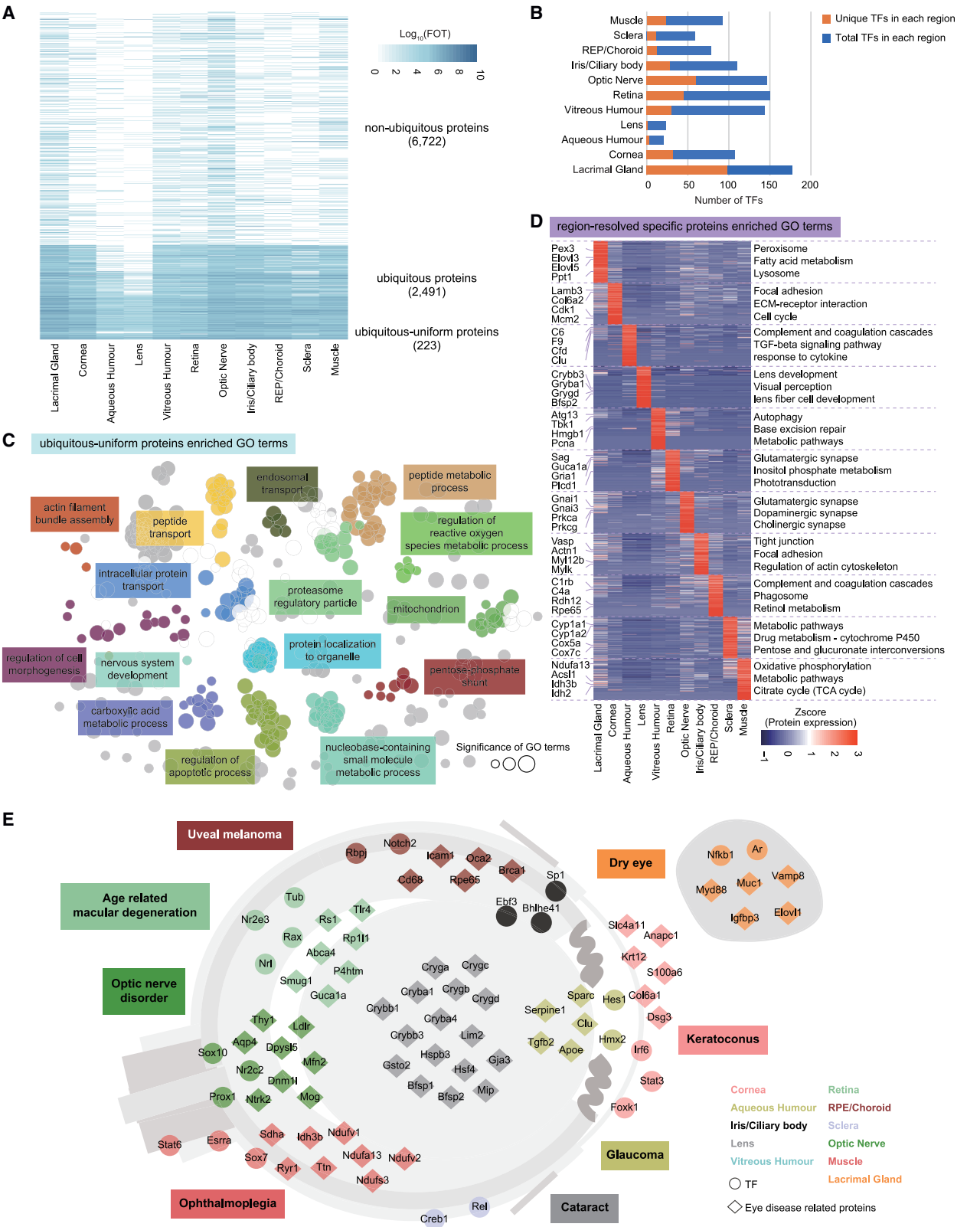

(legend on next page)

employed the TF downstream target gene database from CellNET60 with the TF patterns in this study. Nfkb1 and Ar were found to be dominant in the lacrimal gland ($p < 0.05$, fold change > 5) and necessary for control of lacrimal gland function. Their target genes, including Cd14, Mif, Ncoa1, Ptk2, Casp3, etc., whose protein products have been shown to participate in inflammation, cell growth, and apoptosis, were expressed in significant levels in lacrimal gland ($p < 0.05$, fold change > 2). Foxc1 and Stat3, along with their target genes (Egfr, Jak2, Anxa1, C1s, etc.), which maintained corneal transparency and homeostasis, were found to be overrepresented in the cornea ($p < 0.05$, fold change > 2). Hes1 and its target gene Glycam1, which are critical to an association with cell-migratory functions involved in glaucoma, were detected predominantly in aqueous humor ($p < 0.05$, fold change > 5) (Figure 2E).

Comparative proteome analysis between different regions in the mouse eye

For a functional view of the proteomic differences in the mouse eye, we performed the comparison among 11 regions. We determined which proteins are region specific based on the criterion that the expression level of a protein in a certain region was found to be two times greater than the average of the expression levels in all regions (Table S2). The heatmap showed the enrichment analysis of major function pathways of each region using Kyoto Encyclopedia of Genes and Genomes (KEGG) (Figure 2D; Table S2). Peroxisome, fatty acid metabolism, and lysosome-related proteins were enriched in the lacrimal gland, such as Pex3, Elovl3, Elovl5, Ppt1, and others. The main function of the lacrimal gland is the production of lacrimal fluid, which contains antimicrobial agents, including phospholipase, lysozyme, peroxidase, lactoferrin, and immunoglobulins, which provide defense against invading pathogens for cornea.[14] In addition to the lacrimal gland, aqueous humor, vitreous humor, and RPE/choroid were characterized with immune-related pathways. Proteins related with complement and coagulation cascades were enriched in aqueous humor, such as C6, F9, Cfd, and Clu, which were related with AMD.[15] Proteins participating in complement and coagulation cascades were also enriched in RPE/choroid, including C1rb and C4a, associated with choroidal vascular atrophy and RPE changes[16] (Figure 2D; Table S2).

Cornea, lens, vitreous humor, retina, and optic nerve were strongly characterized by visual-function-related pathways. Cornea-region-specific proteins were enriched in focal adhesion, extracellular matrix (ECM)-receptor interaction, and cell cycle, including Clo4a5, Col5a1, Col6a1, Col11a1, and others. Approximately 80% of mass and volume of the cornea consists of a dense, interwoven collagen tissue, which ensures the clearness of light refraction and geometrical properties.[17] Crystallins, such as Cryba1, Cryba4, Crybb1, Crybb3, and Crygd, were enriched in the lens that maintains the transparency and refractive index, and an imbalance in the lenticular proteome is a major contributor to cataract formation.[18] Although vitreous humor is a mixture of 99% water along with proteins, polysaccharides, proteoglycans, and metabolites, we identified proteins involved in autophagy, base excision repair, and metabolism pathways, making the vitreous potentially more biologically active than previously reported.[12,19] Visual transduction-related pathways, such as glutamatergic synapse, inositol phosphate metabolism, and dopaminergic synapse, were enhanced in the retina and optic nerve (Figure 2D; Table S2).

The sclera forms the fibrous coat of the eye with the dense, irregular arrangement of collagen fibrils, provides a tough housing for intraocular contents, and maintains the shape of the eye. In addition, we observed metabolism pathways were enriched in the sclera, such as drug metabolism-cytochrome P450 and pentose and glucuronate interconversions, indicating a promising drug-delivery approach through the sclera. Oxidative phosphorylation and citrate cycle (TCA cycle, tricarboxylic acid cycle)-related proteins were enriched in eye muscle for the maintenance of the shape of the eye and eye movement, including Ndufa13, Acsl1, Idh3b, Idh2, among others (Figure 2D; Table S2).

To gain deeper insights into the association between eye genes and ocular diseases, we matched the region-specific gene lists to the GDA (Gene-Disease Associations) dataset[20] (Figure 2E). Among these associations, many ocular diseases, such as dry eye, keratoconus, glaucoma, cataract, AMD, uveal melanoma, optic nerve disorder, and ophthalmoplegia, were highly associated with the physiology and pathology of different eye regions. Lacrimal gland region-specific genes, such as Myd88, Muc1, Vamp8, Lgfbp3, and Elovl1, were involved in dry eye disease (DED), a common and multifactor-induced autoimmune ocular surface disease related with a loss or reduction of tear film.[21–24] The physical composition of the cornea gives it viscoelastic properties, and keratins, collagens, and transporter-like proteins were highly associated with corneal biomechanics.[25] For example, Krt12, Col6a1, and Slc4a11 detected predominantly in the cornea were involved in keratoconus, a thinning corneal dystrophy. Proteins that might influence the development of glaucoma, such as Sparc, Clu, Serpine1, Tgfb2, and Apoe, were aqueous humor region specific, participating in extracellular matrix, intraocular pressure, and lipid transport.[26–29] Crystallins are a collection of structural proteins found in the lens of the eye and can accumulate damage, losing

Figure 2. Spatial diversity of the mouse ocular proteomes

(A) Heatmap for non-ubiquitous, ubiquitous-uniform, or ubiquitous non-uniform proteins. The color bar on the right indicates the relative protein expression abundance.

(B) The bar graph shows the number of region-specific TFs and total TFs identified in different regions. The blue bar graph shows the number of total TFs identified in different regions. The orange bar graph shows the number of region-specific TFs identified in different regions.

(C) GO term enrichment analysis of the core proteome. The colors of the circles represent the GO functional groups. The group leading term is the most significant term of the group. The size of the circles reflects the statistical significance of the terms.

(D) Heatmap indicates the expression patterns of proteins that were significantly upregulated in the 11 regions, respectively. The color bar on the right indicates the relative protein expression abundance.

(E) Overview of enriched region-specific TFs and eye-disease-related proteins.

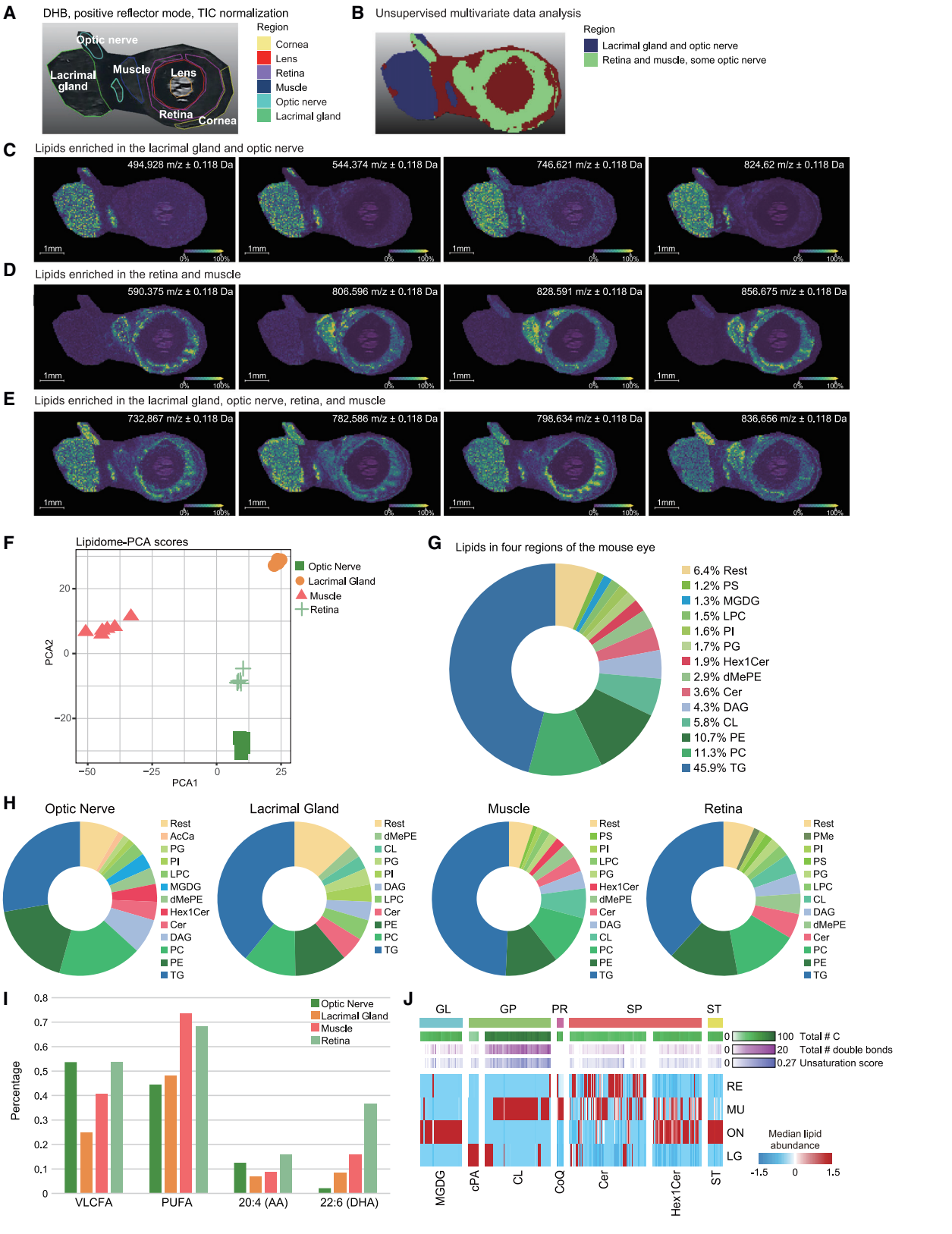

(legend on next page)

their native structure and fusing together to form aggregates, ultimately leading to the development of cataracts.[18] In addition to crystallins, heat shock proteins, Hspb3 and Hsf4, filensins, Bfsp1 and Bfsp2, and lens fiber intrinsic protein, Mip and Lim2, enriched in lens, are also involved in the development of cataracts.[30–33] AMD-associated proteins, such as Rs1, Abca4, Smug1, Tlr4, and Guca1a, were retina region specific (Figure 2E).

Furthermore, we performed IHC staining to validate the differential expression patterns of region-specific proteins (Figure S3A). We randomly selected lacrimal gland-specific proteins (Myd88 and Ar), muscle-specific protein (Ryr1), retina-specific protein (Abca4), and RPE-specific protein (Rpe65) to validate their expression in specific regions by IHC staining. As a result, consistent with our proteomic data, Myd88 and Ar were confirmed to be overrepresented in the lacrimal gland, Ryr1 was enriched in muscle, Abca4 was overrepresented in the retina, and Rpe65 was confirmed to be region specific in RPE (Figure S3A).

MALDI-TOF imaging and region-resolved lipidome of the mouse eye

The eye is one of the organs with high lipid content, which is consistent with our spectra imaging. Furthermore, we investigated lipid expression spatially on the ultrafleXtreme MALDI-TOF/TOF imaging system from 300 to 1,300 m/z (Figures 3A and S4A). We applied dihydroxybenzoic acid solution (DHB) as the matrix deposition on the lipids. We performed unsupervised multivariate data analysis: bisecting k-means clustering across six main regions on the slides, cornea, lens, retina, eye muscle, optic nerve, and lacrimal gland (Figure 3B). Distinctive anatomical structures were successfully differentiated by lipids, indicating the similarity and difference across the mouse eye regions (Figures 3B and S4B).

To compare lipid abundance data from the whole mouse eye regions, we used a ROC (receiver operating characteristic) curve approach to evaluate m/z value based on its discriminating power. Area under the curve (AUC) values between 0 and 1 were obtained for each m/z value describing a signal's discriminatory power based on its normalized relative abundance. With an AUC $\geq$ 0.70 being required for a peak, it was considered statistically significant. We observed some lipids were highly expressed in the optic nerve and lacrimal gland, such as 494.928, 544.374, 746.621, and 824.62 m/z (Figures 3C, S4C, and S4F). Lipids in the retina and eye muscle showed some similarity, such as 590.375, 0.596, 798.634, and 836.656 m/z (Figures 3D and S4D). We also observed that some lipids were presented in all regions, such as 732.867, 782.586, 798.634, and 836.656 m/z (Figures 3E and S4E).

To settle down the identification of region-specific lipids, we further performed the MS/MS analysis on the lipids of four mouse eye regions. We identified a total of 3,739 lipids in the four mouse eye regions, and 1,469 lipids in optic nerve, 819 lipids in lacrimal gland, 2,416 lipids in muscle, and 1,489 lipids in retina (Table S3). A PCA was used to visualize variation and to highlight robust patterns in the datasets in a two-dimensional score plot (Figure 3F). The biological replicates clearly clustered together, demonstrating excellent technical and biological reproducibility. We identified the lipid m/z 798.6338 in imaging mass spectrometry (IMS) was likely to be phosphatidylcholine (PC; 20:1_18:1; m/z 798.6) highly expressed in the four mouse eye regions, the most abundant phospholipid in cells.[34]

Triglycerides (TGs), PCs, and phosphatidylethanolamines (PEs) accounted for a large amount of mouse eye lipids (Figures 3G and 3H). In addition to TGs, PCs, and PEs, diacylglycerols (DAGs), ceramides (Cers), and monohexosylceramides (Hex1Cers) also occupied some proportion of the optic nerve lipidome, which was significant for signal transduction. We found eye muscle was composed of quite a few cardiolipins (CLs), a unique mitochondrial phospholipid that was a critical determinant of mitochondrial function.[35] For the retina, we observed Cers were the maximum lipid class next to TGs, PCs, and PEs (Figure 3H). We further investigated the proportion of very long-chain fatty acids (VLCFAs) and polyunsaturated fatty acids (PUFAs) containing lipids in the four regions. We found the retina was enriched with VLCFAs and PUFAs, especially the 22:6 (likely docosahexaenoic acid [DHA])-containing lipids, which could enhance membrane fluidity and help maintain the highly curved membrane disks of the photoreceptor outer segments[36,37] (Figure 3I).

Furthermore, we identified 1,678 lipids that were differentially abundant across the four mouse eye regions (Kruskal-Wallis, $p < 0.05$; Table S3). The optic nerve was enriched for DAGs, Hex1Cers, and sterol lipids (STs) (Figure 3J). The lacrimal gland demonstrated elevated abundance of TGs and cyclic phosphatidic acids (cPA). The eye muscle exhibited significantly increased levels of TGs, CLs, and coenzyme Q (CoQ). The retina was enriched for TGs and Cers (Figure 3J).

In summary, we conducted MALDI-TOF imaging and found optic nerve, lacrimal gland, eye muscle, and retina had high lipid content compared with other eye regions. Furthermore, lipidome-based comparative analysis across the main four mouse

Figure 3. MALDI-TOF imaging and region-resolved lipidome of the mouse eye

(A) Six distinctive mouse eye regions were illustrated in the MALDI-TOF imaging.

(B) Unsupervised multivariate data analysis: bisecting k-means clustering by lipid expression was performed across six main regions on the slides, cornea, lens, retina, eye muscle, optic nerve, and lacrimal gland.

(C) Lipids enriched in the lacrimal gland and some optic nerve.

(D) Lipids enriched in the retina and muscle.

(E) Lipids enriched in the lacrimal gland, optic nerve, retina, and muscle.

(F) PCA of the lipidome of four mouse brain regions: optic nerve, lacrimal gland, eye muscle, and retina.

(G) Distribution of the 13 most abundant lipid classes in the mouse eye, displayed as parts of the whole.

(H) Distribution of the most abundant lipid classes in the four mouse eye regions, respectively, displayed as parts of the whole.

(I) The bar plot represents the percentage of very long-chain fatty acid- (VLCFA), polyunsaturated fatty acid- (PUFA), the 20:4- (likely arachidonic acid [AA]), and the 22:6-containing (likely docosahexaenoic acid [DHA]) lipids in the four mouse eye regions.

(J) Abundance of differentially expressed lipids detected across the four mouse eye regions.

regions revealed the distinguished and significant lipid classes contributed in each region.

Distinct lipid-related proteome of the mouse eye

We further investigated whether the differences in lipid metabolic pathways are also detectable on the proteome level. We used the proteomic data of the four mouse eye regions—optic nerve, lacrimal gland, muscle, and retina—for clustering and cluster-specific enrichment analysis of lipid-related metabolic pathways using KEGG (Figure 4A). Lipid-related pathways enriched in eye muscle (module 4) included fatty acid metabolism, metabolism of cofactors, TG metabolism, among others (Figure 4B). For example, coenzymes, Coq3, Coq7, and Coq9, were highly expressed in eye muscle (Figure 4C). For the optic nerve, we found phospholipid metabolism- and phosphatidylinositol phosphate metabolism-related proteins were enriched in the optic nerve (module 1), such as phospholipase C (Plcb4, Plcd3, and Plch2) and phosphatidylinositol phosphate kinase (Pi4ka, Pip4k2b, Pip5k1a, and Pip5k1b) (Figures 4B and 4C). Pathways enriched in lacrimal gland involved fatty acid metabolism, phospholipid metabolism, and glycerophospholipid metabolism (modules 5 and 3) (Figure 4B). The abundance of elongation of VLCFAs protein (Elovl1, Elovl3, Elovl5, and Elovl6) and peroxisomal acyl-coenzyme A oxidase was elevated in the lacrimal gland (Acox1, Acox2, and Acox3) (Figure 4C). For the retina, we observed that phospholipid metabolism, phosphatidylinositol phosphate metabolism, sphingolipid metabolism, and steroids metabolism were enriched in the retina (module 2), and a Cer synthase, Cers2, was highly expressed in the retina (Figures 4B and 4C).

We explored the connection between the differential abundance of VLCFA-containing TGs, CLs, CoQs, Cers, and Hex1Cers and their metabolically related enzymes and kinases. A co-regulation was shown with VLCFA-containing TGs and elongation of VLCFAs protein (Elovl1, Elovl3, Elovl5, and Elovl6) in the lacrimal gland, which might function in the prevention of DED in mice[38] (Figure 4D). Protein expression of coenzymes (Coq3, Coq5, Coq7, and Coq9) showed significant correlation with the lipid abundance of CoQs (CoQ6, CoQ7, CoQ8, and CoQ9) and CLs in the eye muscle. In the retina, a co-regulation was shown with Cers and Cers2 (Cer synthase 2). Gba2 (glucosylceramidase beta 2) was significantly upregulated only in the optic nerve and correlated with Hex1Cers, which were related to glaucoma[39] (Figure 4D). In brief, the clustering and cluster-specific enrichment analysis revealed the major lipid metabolism pathways and region-specific protein-lipid connections functioning in the optic nerve, lacrimal gland, eye muscle, and retina.

Network between proteome and lipidome in the mouse eye was verified by phosphoproteome

To verify our findings of region-specific protein-lipid connections, we further quantified the phosphoprotein expression across the four main mouse eye regions (Table S5). We determined which phosphoproteins are region specific based on the criterion that the expression level of a phosphoprotein in a certain region was found to be two times greater than the average of the expression levels in all regions. We found that the Ras signaling pathway, calcium signaling pathway, and endocytosis were enriched in the optic nerve (Figure 5A). The lacrimal gland demonstrated elevated abundance of phosphoproteins participating in peroxisome and fatty acid metabolism. As for the eye muscle, citrate cycle- (TCA cycle) and oxidative phosphorylation-related phosphoproteins were highly expressed. Glutamatergic synapse and synaptic vesicle cycle pathways were enriched in the retina (Figure 5A).

In the eye muscle, Coq9 (mitochondrial 5-demethoxyubiquinone hydroxylase) demonstrated elevated abundance at proteomic and phosphoproteomic expression levels, involved with CoQ biosynthesis that is an essential component of the respiratory chain[40] (Figures 3H and 5B). CL is also found almost in mitochondria and contains almost exclusively 18-carbon fatty acids, and 80% of this is typically linoleic acids (18:2(n−6)), such as CL (18:2_18:2_18:2_18:2) and CL (18:2_18:1_18:2_18:2), which were enriched in the eye muscle in our data[41] (Figures 4D and 5B). We observed that peroxisomal biogenesis factors (Pex1 and Pex14), acyl-CoA oxidases (Acox1 and Acox2), and ATP binding cassette subfamily D member 3 (Abcd3) were enriched in the lacrimal gland at proteomic and phosphoproteomic expression levels (Figures 3H and 5B). Although mitochondria are the main site of oxidation of long-chain fatty acids, our findings indicated that peroxisomes might also catalyze the β-oxidation of VLCFAs in the lacrimal gland.[42]

We found that the retina and optic nerve were enriched for phosphatidylinositol phosphate metabolism (Figure 3H). Therefore, we further investigated phosphoinositide signaling-related kinases in the retina and optic nerve. Pik3c2b, Pik3c3, and Pip4k2a were upregulated in the retina, which mediated formation of phosphatidylinositol 3,4-phosphate (PI(3,4)P2) functioning in clathrin-mediated endocytosis[43] (Figure 5B). The optic nerve demonstrated elevated expression of Pi4ka and Pip5k1a catalyzing the biosynthesis of phosphatidylinositol 4,5-bisphosphate (PI(4,5)P2), a lipid second messenger that regulates several cellular processes, such as signal transduction, vesicle trafficking, and others.[44] In summary, our phosphoproteomic data across the four main mouse eye regions verified our findings of region-specific protein-lipid connections, indicating our data could further serve as a promising database for ocular studies.

DISCUSSION

The organs are constituted of different cell types that construct in a precise temporal-spatial order. Because of the remarkable improvement in MS techniques, the organ/tissue proteome achieved in-depth coverage, which made it a powerful tool to decipher the complex molecular features of the organ. To date, the cell-type-resolved liver proteome[45] and cell-type/region-resolved brain proteome[46] were described. As the important part of studying the ocular function, the region-resolved multi-omics profiling of the eye is comparatively lacking. In this study, we established the first spatial-resolved multi-omics map of the healthy mouse eye. We quantified over 13,000 proteins, representing by far the deepest proteome of the healthy mouse eye. Our datasets provide a navigation tool to connect the proteome expression to the anatomy of the mouse eye. The depth coverage of aqueous humor, vitreous humor, and REP/choroid proteins in our study provides a great potential contrast to investigate immunological homeostasis of the eye and autoimmune or

CellPress
OPEN ACCESS

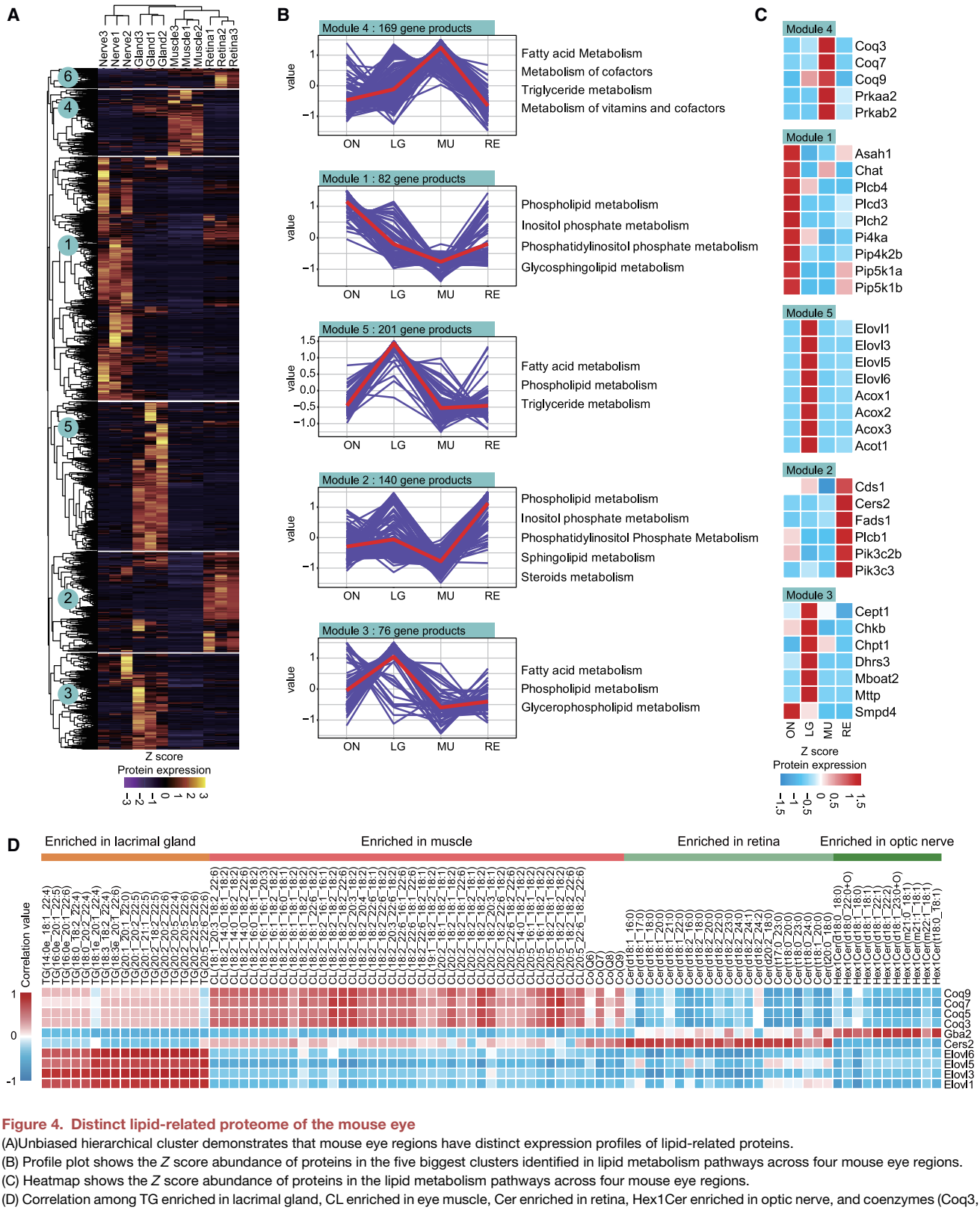

Figure 4. Distinct lipid-related proteome of the mouse eye

(A)Unbiased hierarchical cluster demonstrates that mouse eye regions have distinct expression profiles of lipid-related proteins.

(B) Profile plot shows the *Z* score abundance of proteins in the five biggest clusters identified in lipid metabolism pathways across four mouse eye regions.

(C) Heatmap shows the *Z* score abundance of proteins in the lipid metabolism pathways across four mouse eye regions.

(D) Correlation among TG enriched in lacrimal gland, CL enriched in eye muscle, Cer enriched in retina, Hex1Cer enriched in optic nerve, and coenzymes (Coq3, Coq5, Coq7, and Coq9), ceramide synthase (Cers2), glucosylceramidase beta 2 (Gba2), and elongation of very long chain fatty acids protein (Elovl1, Elovl3, Elovl5, and Elovl6).

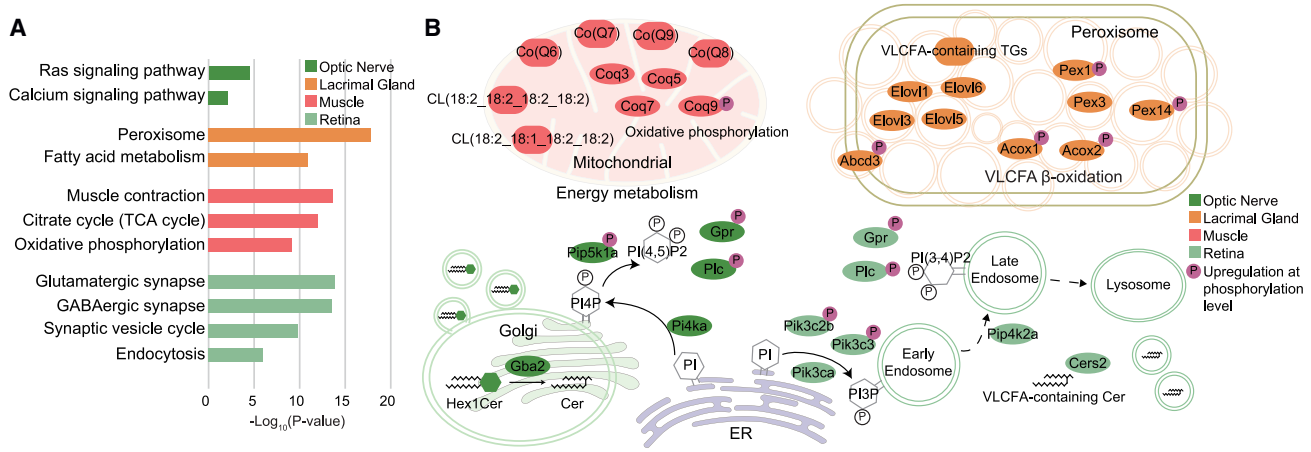

Figure 5. Network between proteome and lipidome in the mouse eye was verified by phosphoproteome

(A) The bar plot represented $-\mathrm{Log}_{10}$(p value) of the main enriched pathways based on phosphoproteomic data in the four mouse eye regions.

(B) The diagram showed the main region-specific protein-lipid connections in the four mouse eye regions verified by phosphoproteomic data.

infection-related immune diseases. Proteome-based comparative analysis across the 11 mouse regions revealed the distinguished and significant protein pathways functioning in each region.

Importantly, taking advantage of IMS, which allows unsupervised and simultaneous analyses of molecules (e.g., metabolites, proteins, and lipids) *in situ* on a single tissue section,[47] we presented the distribution of lipids and proteins preserving their spatial coordinates and generating a molecular intensity map reflecting the relative molecule abundance. These data could serve as recourse to decipher clear divisions of labor in the biological pathways of eyes. Moreover, proteome combined with image technologies uncovered key molecular features of each region. We observed elevated enrichment of lipids in the retina, eye muscle, optic nerve, and lacrimal gland. Based on the findings, we further performed region-resolved quantitative lipid analysis of the eye regions and characterized fatty acid chain length and saturation. Comparative analysis of the mouse eye proteome and lipidome landscapes captured the heterogeneity of mouse eye regions, profiled the characteristic protein and lipid metabolism pathways, and suggested the involvement of the metabolic process in the functional regulation of their regions.

In our study, we identified some proteins and lipids implicated in the signaling pathway of ocular disease, such as keratoconus, glaucoma, cataract, AMD, dry eye, and so on. We found VLCFA- and PUFA-containing lipids occupied a relatively large proportion in the mouse eye lipids. The 22:6 (likely DHA)-containing lipids were most enriched in the retina in the mouse eye regions, bolstering survival of the photoreceptor cells and against retinopathy.[48] The lacrimal gland was well known as the producer of tears. In addition to antimicrobial agents, VLCFA-containing lipids and elongation of VLCFA proteins (Elovl1, Elovl3, Elovl5, and Elovl6) showed a co-upregulation in the lacrimal gland in our study, which was important for the prevention of DED.[38] In our data, eye muscle was characterized as oxidative phosphorylation and citrate cycle (TCA cycle). CoQ lipid and CL were also significantly enriched in the eye muscle, located mainly in mitochondria, and function in electron transport, oxidative phosphorylation, and ATP synthesis.[41,49,50] Mitochondrial disease is a heterogeneous group of energy metabolism disorders presenting across all ages with a wide range of ocular manifestations.[51] Energy metabolism in eye muscle is notable and inextricably linked with extraocular muscle disorders.

In summary, the region-resolved mouse eye proteome and lipidome provide a physiological reference map that may be useful in clinical applications. Results from multiple bioinformatics analysis enable us to better understand the relationship between biological function, molecule mechanism, and disease development in ocular disease proteins, which may help other researchers to develop comprehensive cognition on physiology and etiology studies regarding ocular proteins and lipids.

Limitations of the study

In this study, we established the first spatial-resolved multi-omics map of the healthy mouse eye, thus contributing to the investigation of ocular disease. Even though we have tried to collect as many anatomical regions of mouse eye as we can, more meticulous anatomical regions still need to be investigated and characterized, such as lens epithelial cells, the trabecular meshwork, the fovea centralis, among others. These regions usually occupy a very small volume in the eyes, although it has been reported that they play extremely important roles in ocular disease.[52,53]

STAR★METHODS

Detailed methods are provided in the online version of this paper and include the following:

- KEY RESOURCES TABLE
- RESOURCE AVAILABILITY
  - Lead contact
  - Materials availability
  - Data and code availability

SUPPLEMENTAL INFORMATION

Supplemental information can be found online at https://doi.org/10.1016/j.celrep.2023.112121.

ACKNOWLEDGMENTS

This work was supported by the National Key R&D Program of China (2022YFA1303200, 2022YFA1303201, 2017YFA0505102, 2016YFA0502500, 2018YFA0507501, 2017YFC0908404, 2020YFE0201600, 2018YFE0201600, 2018YFE0201603, 2018YFA0507500, 2018YFA0507501, 2017YFA0505100, and 2017YFA0505101), National Natural Science Foundation of China (31770886, 31972933, 31700682, and 32201212), Shanghai Municipal Science and Technology Major Project (2017SHZDZX01), Shuguang Program of Shanghai Education Development Foundation and Shanghai Municipal Education Commission (19SG02), Program of Shanghai Academic/Technology Research Leader (22XD1420100), Major Project of Special Development Funds of Zhangjiang National Independent innovation Demonstration Zone (ZJ2019-ZD-004), China Postdoctoral Science Foundation (2019M651268), National Postdoctoral Program for Innovative Talents, and the Fudan original research personalized support project. We would like to thank Bruker Daltonics, Bruker Singapore Pte Ltd, and Bruker Shanghai, China for the MALDI-TOF imaging analysis, and we are grateful to Wen Donq Looi and Xianming Liu for their help.

AUTHOR CONTRIBUTIONS

Conceptualization, C.D. and M.J.; investigation, H.X., B.Z., Y.W., N.X., F.Z., and R.L.; formal analysis and visualization, H.X.; writing – original draft, H.X.; writing – review & editing, H.X., C.D., and M.J.; funding acquisition, C.D.

DECLARATION OF INTERESTS

The authors declare no competing interests.

INCLUSION AND DIVERSITY

We support inclusive, diverse, and equitable conduct of research.

Received: June 28, 2022
Revised: December 19, 2022
Accepted: January 31, 2023

REFERENCES

1. Webson, A. (2021). Eye health and the decade of action for the sustainable development goals. Lancet Global Health *9*, e383–e384. https://doi.org/10.1016/S2214-109X(21)00035-8.
2. Bron, A.J., de Paiva, C.S., Chauhan, S.K., Bonini, S., Gabison, E.E., Jain, S., Knop, E., Markoulli, M., Ogawa, Y., Perez, V., et al. (2017). TFOS DEWS II pathophysiology report. Ocul. Surf. *15*, 438–510. https://doi.org/10.1016/j.jtos.2017.05.011.
3. Winiarczyk, M., Kaarniranta, K., Winiarczyk, S., Adaszek, Ł., Winiarczyk, D., and Mackiewicz, J. (2018). Tear film proteome in age-related macular degeneration. Graefes Arch. Clin. Exp. Ophthalmol. *256*, 1127–1139. https://doi.org/10.1007/s00417-018-3984-y.
4. Rinsky, B., Beykin, G., Grunin, M., Amer, R., Khateb, S., Tiosano, L., Almeida, D., Hagbi-Levi, S., Elbaz-Hayoun, S., and Chowers, I. (2021). Analysis of the aqueous humor proteome in patients with age-related macular degeneration. Invest. Ophthalmol. Vis. Sci. *62*, 18. https://doi.org/10.1167/iovs.62.10.18.
5. Zhang, L., Wu, Y., Zheng, B., Su, L., Chen, Y., Ma, S., Hu, Q., Zou, X., Yao, L., Yang, Y., et al. (2019). Rapid histology of laryngeal squamous cell carcinoma with deep-learning based stimulated Raman scattering microscopy. Theranostics *9*, 2541–2554. https://doi.org/10.7150/thno.32655.
6. Zhang, B., Xu, H., Chen, J., Zhu, X., Xue, Y., Yang, Y., Ao, J., Hua, Y., and Ji, M. (2021). Highly specific and label-free histological identification of microcrystals in fresh human gout tissues with stimulated Raman scattering. Theranostics *11*, 3074–3088. https://doi.org/10.7150/thno.53755.
7. Saar, B.G., Freudiger, C.W., Reichman, J., Stanley, C.M., Holtom, G.R., and Xie, X.S. (2010). Video-rate molecular imaging in vivo with stimulated Raman scattering. Science *330*, 1368–1370. https://doi.org/10.1126/science.1197236.
8. Giansanti, P., Samaras, P., Bian, Y., Meng, C., Coluccio, A., Frejno, M., Jakubowsky, H., Dobiasch, S., Hazarika, R.R., Rechenberger, J., et al. (2022). Mass spectrometry-based draft of the mouse proteome. Nat. Methods *19*, 803–811. https://doi.org/10.1038/s41592-022-01526-y.
9. Ahmad, M.T., Zhang, P., Dufresne, C., Ferrucci, L., and Semba, R.D. (2018). The human eye proteome Project: updates on an emerging proteome. Proteomics *18*, e1700394. https://doi.org/10.1002/pmic.201700394.
10. Hubens, W.H.G., Mohren, R.J.C., Liesenborghs, I., Eijssen, L.M.T., Ramdas, W.D., Webers, C.A.B., and Gorgels, T.G.M.F. (2020). The aqueous humor proteome of primary open angle glaucoma: an extensive review. Exp. Eye Res. *197*, 108077. https://doi.org/10.1016/j.exer.2020.108077.
11. Zhang, P., Kirby, D., Dufresne, C., Chen, Y., Turner, R., Ferri, S., Edward, D.P., Van Eyk, J.E., and Semba, R.D. (2016). Defining the proteome of human iris, ciliary body, retinal pigment epithelium, and choroid. Proteomics *16*, 1146–1153. https://doi.org/10.1002/pmic.201500188.
12. Mohanty, V., Pinto, S.M., Subbannayya, Y., Najar, M.A., Murthy, K.B., Prasad, T.S.K., and Murthy, K.R. (2020). Digging deeper for the eye proteome in vitreous substructures: a high-resolution proteome map of the normal human vitreous base. OMICS *24*, 379–389. https://doi.org/10.1089/omi.2020.0020.
13. Skeie, J.M., and Mahajan, V.B. (2014). Proteomic landscape of the human choroid-retinal pigment epithelial complex. JAMA Ophthalmol. *132*, 1271–1281. https://doi.org/10.1001/jamaophthalmol.2014.2065.
14. Conrady, C.D., Joos, Z.P., and Patel, B.C.K. (2016). Review: the lacrimal gland and its role in dry eye. J. Ophthalmol. *2016*, 7542929. https://doi.org/10.1155/2016/7542929.
15. de Jong, S., Gagliardi, G., Garanto, A., de Breuk, A., Lechanteur, Y.T.E., Katti, S., van den Heuvel, L.P., Volokhina, E.B., and den Hollander, A.I. (2021). Implications of genetic variation in the complement system in

age-related macular degeneration. Prog. Retin. Eye Res. *84*, 100952. https://doi.org/10.1016/j.preteyeres.2021.100952.

16. Yang, X., Zhao, L., Campos, M.M., Abu-Asab, M., Ortolan, D., Hotaling, N., Bharti, K., and Wong, W.T. (2020). CSF1R blockade induces macrophage ablation and results in mouse choroidal vascular atrophy and RPE disorganization. Elife *9*, e55564. https://doi.org/10.7554/elife.55564.
17. Kang, B.S., Lam, T.C., Cheung, J.K.-W., Li, K.K., and Kee, C.-S. (2021). Corneal proteome and differentially expressed corneal proteins in highly myopic chicks using a label-free SWATH-MS quantification approach. Sci. Rep. *11*, 5495. https://doi.org/10.1038/s41598-021-84904-4.
18. Andley, U.P. (2007). Crystallins in the eye: function and pathology. Prog. Retin. Eye Res. *26*, 78–98. https://doi.org/10.1016/j.preteyeres.2006.10.003.
19. Aretz, S., Krohne, T.U., Kammerer, K., Warnken, U., Hotz-Wagenblatt, A., Bergmann, M., Stanzel, B.V., Kempf, T., Holz, F.G., Schnölzer, M., and Kopitz, J. (2013). In-depth mass spectrometric mapping of the human vitreous proteome. Proteome Sci. *11*, 22. https://doi.org/10.1186/1477-5956-11-22.
20. Piñero, J., Ramírez-Anguita, J.M., Saüch-Pitarch, J., Ronzano, F., Centeno, E., Sanz, F., and Furlong, L.I. (2020). The DisGeNET knowledge platform for disease genomics: 2019 update. Nucleic Acids Res. *48*, D845–D855. https://doi.org/10.1093/nar/gkz1021.
21. Watanabe, K., Yoshida, M., Okumura, T., Sassa, T., Kihara, A., and Uchiyama, A. (2021). Improvement of evaporative dry eye with meibomian gland dysfunction in model mice by treatment with ophthalmic solution containing mineral oil. Transl. Vis. Sci. Technol. *10*, 21. https://doi.org/10.1167/tvst.10.4.21.
22. Reins, R.Y., Lema, C., Courson, J., Kunnen, C.M.E., and Redfern, R.L. (2018). MyD88 deficiency protects against dry eye-induced damage. Invest. Ophthalmol. Vis. Sci. *59*, 2967–2976. https://doi.org/10.1167/iovs.17-23397.
23. Portal, C., Gouyer, V., Gottrand, F., and Desseyn, J.-L. (2019). Ocular mucins in dry eye disease. Exp. Eye Res. *186*, 107724. https://doi.org/10.1016/j.exer.2019.107724.
24. Fukui, M., Ogawa, Y., Mukai, S., Kamoi, M., Asato, T., Kawakami, Y., and Tsubota, K. (2017). Reduced expression of VAMP8 in lacrimal gland affected by chronic Graft-versus-host disease. J. Ophthalmol. *2017*, 1639012. https://doi.org/10.1155/2017/1639012.
25. Chaerkady, R., Shao, H., Scott, S.-G., Pandey, A., Jun, A.S., and Chakravarti, S. (2013). The keratoconus corneal proteome: loss of epithelial integrity and stromal degeneration. J. Proteonomics *87*, 122–131. https://doi.org/10.1016/j.jprot.2013.05.023.
26. Copin, B., Brézin, A.P., Valtot, F., Dascotte, J.-C., Béchetoille, A., and Garchon, H.-J. (2002). Apolipoprotein E-promoter single-nucleotide polymorphisms affect the phenotype of primary open-angle glaucoma and demonstrate interaction with the myocilin gene. Am. J. Hum. Genet. *70*, 1575–1581. https://doi.org/10.1086/340733.
27. Lv, Y., Zhang, Z., Xing, X., and Liu, A. (2020). lncRNA TGFβ2-AS1 promotes ECM production via TGF-β2 in human trabecular meshwork cells. Biochem. Biophys. Res. Commun. *527*, 881–888. https://doi.org/10.1016/j.bbrc.2020.05.003.
28. Fini, M.E., Jeong, S., and Wilson, M.R. (2020). Therapeutic potential of the molecular chaperone and matrix metalloproteinase inhibitor clusterin for dry eye. Int. J. Mol. Sci. *22*, 116. https://doi.org/10.3390/ijms22010116.
29. Chen, L.J., Tam, P.O.S., Tham, C.C.Y., Liang, X.Y., Chiang, S.W.Y., Canlas, O., Ritch, R., Rhee, D.J., and Pang, C.P. (2010). Evaluation of SPARC as a candidate gene of juvenile-onset primary open-angle glaucoma by mutation and copy number analyses. Mol. Vis. *16*, 2016–2025.
30. Boncoraglio, A., Minoia, M., and Carra, S. (2012). The family of mammalian small heat shock proteins (HSPBs): implications in protein deposit diseases and motor neuropathies. Int. J. Biochem. Cell Biol. *44*, 1657–1669. https://doi.org/10.1016/j.biocel.2012.03.011.
31. Tapodi, A., Clemens, D.M., Uwineza, A., Jarrin, M., Goldberg, M.W., Thinon, E., Heal, W.P., Tate, E.W., Nemeth-Cahalan, K., Vorontsova, I., et al. (2019). BFSP1 C-terminal domains released by post-translational processing events can alter significantly the calcium regulation of AQP0 water permeability. Exp. Eye Res. *185*, 107585. https://doi.org/10.1016/j.exer.2019.02.001.
32. Zhou, Z., Wang, B., Luo, Y., Zhou, G., Hu, S., Zhang, H., Ma, X., and Qi, Y. (2011). Major intrinsic protein (MIP) polymorphism is associated with age-related cataract in Chinese. Mol. Vis. *17*, 2292–2296.
33. Zhou, Z., Wang, B., Hu, S., Zhang, C., Ma, X., and Qi, Y. (2011). Genetic variations in GJA3, GJA8, LIM2, and age-related cataract in the Chinese population: a mutation screening study. Mol. Vis. *17*, 621–626.
34. Cole, L.K., Vance, J.E., and Vance, D.E. (2012). Phosphatidylcholine biosynthesis and lipoprotein metabolism. Biochim. Biophys. Acta *1821*, 754–761. https://doi.org/10.1016/j.bbalip.2011.09.009.
35. Fajardo, V.A., Mikhaeil, J.S., Leveille, C.F., Saint, C., and LeBlanc, P.J. (2017). Cardiolipin content, linoleic acid composition, and tafazzin expression in response to skeletal muscle overload and unload stimuli. Sci. Rep. *7*, 2060. https://doi.org/10.1038/s41598-017-02089-1.
36. Bennett, L.D., Hopiavuori, B.R., Brush, R.S., Chan, M., Van Hook, M.J., Thoreson, W.B., and Anderson, R.E. (2014). Examination of VLC-PUFA-deficient photoreceptor terminals. Invest. Ophthalmol. Vis. Sci. *55*, 4063–4072. https://doi.org/10.1167/iovs.14-13997.
37. Hopiavuori, B.R., Anderson, R.E., and Agbaga, M.-P. (2019). ELOVL4: very long-chain fatty acids serve an eclectic role in mammalian health and function. Prog. Retin. Eye Res. *69*, 137–158. https://doi.org/10.1016/j.preteyeres.2018.10.004.
38. Sassa, T., Tadaki, M., Kiyonari, H., and Kihara, A. (2018). Very long-chain tear film lipids produced by fatty acid elongase ELOVL1 prevent dry eye disease in mice. Faseb. J. *32*, 2966–2978. https://doi.org/10.1096/fj.201700947r.
39. Chauhan, M.Z., Valencia, A.-K., Piqueras, M.C., Enriquez-Algeciras, M., and Bhattacharya, S.K. (2019). Optic nerve lipidomics reveal impaired glucosylsphingosine lipids pathway in glaucoma. Invest. Ophthalmol. Vis. Sci. *60*, 1789–1798. https://doi.org/10.1167/iovs.18-25802.
40. Martín-Montalvo, A., González-Mariscal, I., Padilla, S., Ballesteros, M., Brautigan, D.L., Navas, P., and Santos-Ocaña, C. (2011). Respiratory-induced coenzyme Q biosynthesis is regulated by a phosphorylation cycle of Cat5p/Coq7p. Biochem. J. *440*, 107–114. https://doi.org/10.1042/bj20101422.
41. Basu Ball, W., Neff, J.K., and Gohil, V.M. (2018). The role of nonbilayer phospholipids in mitochondrial structure and function. FEBS Lett. *592*, 1273–1290. https://doi.org/10.1002/1873-3468.12887.
42. Wanders, R.J.A., Vaz, F.M., Waterham, H.R., and Ferdinandusse, S. (2020). Fatty acid oxidation in peroxisomes: enzymology, metabolic crosstalk with other organelles and peroxisomal disorders. Adv. Exp. Med. Biol. *1299*, 55–70. https://doi.org/10.1007/978-3-030-60204-8_5.
43. Gozzelino, L., De Santis, M.C., Gulluni, F., Hirsch, E., and Martini, M. (2020). PI(3,4)P2 signaling in cancer and metabolism. Front. Oncol. *10*, 360. https://doi.org/10.3389/fonc.2020.00360.
44. Liu, B., and Guo, X. (2021). Disarming PI(4,5)P2 in the plasma membrane. Native Plants *7*, 552–553. https://doi.org/10.1038/s41477-021-00902-4.
45. Ding, C., Li, Y., Guo, F., Jiang, Y., Ying, W., Li, D., Yang, D., Xia, X., Liu, W., Zhao, Y., et al. (2016). A cell-type-resolved liver proteome. Mol. Cell. Proteomics *15*, 3190–3202. https://doi.org/10.1074/mcp.m116.060145.
46. Jung, S.Y., Choi, J.M., Rousseaux, M.W.C., Malovannaya, A., Kim, J.J., Kutzera, J., Wang, Y., Huang, Y., Zhu, W., Maity, S., et al. (2017). An anatomically resolved mouse brain proteome reveals Parkinson disease-relevant pathways. Mol. Cell. Proteomics *16*, 581–593. https://doi.org/10.1074/mcp.M116.061440.
47. Angel, P.M., and Caprioli, R.M. (2013). Matrix-assisted laser desorption ionization imaging mass spectrometry: in situ molecular mapping. Biochemistry *52*, 3818–3828. https://doi.org/10.1021/bi301519p.

48. Knott, E.J., Gordon, W.C., Jun, B., Do, K., and Bazan, N.G. (2018). Retinal pigment epithelium and photoreceptor preconditioning protection requires docosanoid signaling. Cell. Mol. Neurobiol. *38*, 901–917. https://doi.org/10.1007/s10571-017-0565-2.

49. Stefely, J.A., and Pagliarini, D.J. (2017). Biochemistry of mitochondrial coenzyme Q biosynthesis. Trends Biochem. Sci. *42*, 824–843. https://doi.org/10.1016/j.tibs.2017.06.008.

50. Subramanian, K., Jochem, A., Le Vasseur, M., Lewis, S., Paulson, B.R., Reddy, T.R., Russell, J.D., Coon, J.J., Pagliarini, D.J., and Nunnari, J. (2019). Coenzyme Q biosynthetic proteins assemble in a substrate-dependent manner into domains at ER-mitochondria contacts. J. Cell Biol. *218*, 1353–1369. https://doi.org/10.1083/jcb.201808044.

51. Schrier, S.A., and Falk, M.J. (2011). Mitochondrial disorders and the eye. Curr. Opin. Ophthalmol. *22*, 325–331. https://doi.org/10.1097/icu.0b013e328349419d.

52. Lin, H., Ouyang, H., Zhu, J., Liu, Z., Huang, S., Chen, S., Cao, G., Li, G., Signer, R.A.J., Xu, Y., et al. (2016). Lens regeneration using endogenous stem cells with gain of visual function. Nature *531*, 323–328. https://doi.org/10.1038/nature17181.

53. Buffault, J., Labbé, A., Hamard, P., Brignole-Baudouin, F., and Baudouin, C. (2020). The trabecular meshwork: structure, function and clinical implications. A review of the literature. J. Fr. Ophtalmol. *43*, e217–e230. https://doi.org/10.1016/j.jfo.2020.05.002.

54. Cheng, J.-X., and Xie, X.S. (2015). Vibrational spectroscopic imaging of living systems: an emerging platform for biology and medicine. Science *350*, aaa8870. https://doi.org/10.1126/science.aaa8870.

55. Freudiger, C.W., Min, W., Saar, B.G., Lu, S., Holtom, G.R., He, C., Tsai, J.C., Kang, J.X., and Xie, X.S. (2008). Label-free biomedical imaging with high sensitivity by stimulated Raman scattering microscopy. Science *322*, 1857–1861. https://doi.org/10.1126/science.1165758.

56. Hu, F., Shi, L., and Min, W. (2019). Biological imaging of chemical bonds by stimulated Raman scattering microscopy. Nat. Methods *16*, 830–842. https://doi.org/10.1038/s41592-019-0538-0.

57. Campagnola, P.J., and Loew, L.M. (2003). Second-harmonic imaging microscopy for visualizing biomolecular arrays in cells, tissues and organisms. Nat. Biotechnol. *21*, 1356–1360. https://doi.org/10.1038/nbt894.

58. Cox, G., and Kable, E. (2006). Second-harmonic imaging of collagen. In Methods in Molecular Medicine, D.J. Taatjes and B.T. Mossman, eds., pp. 15–35.

59. Ji, M., Orringer, D.A., Freudiger, C.W., Ramkissoon, S., Liu, X., Lau, D., Golby, A.J., Norton, I., Hayashi, M., Agar, N.Y.R., et al. (2013). Rapid, label-free detection of brain tumors with stimulated Raman scattering microscopy. Sci. Transl. Med. *5*, 201ra119. https://doi.org/10.1126/scitranslmed.3005954.

60. Feng, J., Ding, C., Qiu, N., Ni, X., Zhan, D., Liu, W., Xia, X., Li, P., Lu, B., Zhao, Q., et al. (2017). Firmiana: towards a one-stop proteomic cloud platform for data processing and analysis. Nat. Biotechnol. *35*, 409–412. https://doi.org/10.1038/nbt.3825.

61. Schwanhäusser, B., Busse, D., Li, N., Dittmar, G., Schuchhardt, J., Wolf, J., Chen, W., and Selbach, M. (2011). Global quantification of mammalian gene expression control. Nature *473*, 337–342. https://doi.org/10.1038/nature10098.

62. Mergner, J., Frejno, M., List, M., Papacek, M., Chen, X., Chaudhary, A., Samaras, P., Richter, S., Shikata, H., Messerer, M., et al. (2020). Mass-spectrometry-based draft of the Arabidopsis proteome. Nature *579*, 409–414. https://doi.org/10.1038/s41586-020-2094-2.

63. Thoms, M., Thomson, E., Baßler, J., Gnädig, M., Griesel, S., and Hurt, E. (2015). The exosome is recruited to RNA substrates through specific adaptor proteins. Cell *162*, 1029–1038. https://doi.org/10.1016/j.cell.2015.07.060.

64. Xu, J.-Y., Zhang, C., Wang, X., Zhai, L., Ma, Y., Mao, Y., Qian, K., Sun, C., Liu, Z., Jiang, S., et al. (2020). Integrative proteomic characterization of human lung adenocarcinoma. Cell *182*, 245–261.e17. https://doi.org/10.1016/j.cell.2020.05.043.

65. Taus, T., Köcher, T., Pichler, P., Paschke, C., Schmidt, A., Henrich, C., and Mechtler, K. (2011). Universal and confident phosphorylation site localization using phosphoRS. J. Proteome Res. *10*, 5354–5362. https://doi.org/10.1021/pr200611n.

66. Yamada, T., Uchikata, T., Sakamoto, S., Yokoi, Y., Nishiumi, S., Yoshida, M., Fukusaki, E., and Bamba, T. (2013). Supercritical fluid chromatography/Orbitrap mass spectrometry based lipidomics platform coupled with automated lipid identification software for accurate lipid profiling. J. Chromatogr. A *1301*, 237–242. https://doi.org/10.1016/j.chroma.2013.05.057.

67. Liu, L., and Zhu, S. (2021). Computational Methods for Prediction of Human Protein-Phenotype Associations: A Review. Phenomics. *1*, 171–185. https://doi.org/10.1007/s43657-021-00019-w.

STAR★METHODS

KEY RESOURCES TABLE

REAGENT or RESOURCE	SOURCE	IDENTIFIER
Antibodies		
Myd88	Proteintech	Cat#67969-1-Ig; RRID:AB_2918720
Ar	Proteintech	Cat#22089-1-AP; RRID:AB_11182176
Ryr1	Proteintech	Cat#66539-1-Ig; RRID:AB_2881901
Abca4	Novus Biologicals	Cat#NBP1-30032; RRID:AB_1968439
Rpe65	Proteintech	Cat#17939-1-AP; RRID:AB_2285290
Chemicals, peptides, and recombinant proteins		
Trypsin	Promega	Cat#V528A
Methyl tert-butyl ether (MTBE)	Sigma	Cat# 1634-04-4
Dihydroxybenzoic acid solution (DHB)	Sigma	Cat#63542-76-7
Critical commercial assays		
High-Select™ Fe-NTA Phosphopeptide Enrichment Kit	Thermo scientific	Cat#A32992
Deposited data		
Proteomics data	This paper	iProx: PXD039460 (https://www.iprox.cn)
Phosphoroteomics data	This paper	iProx: PXD039460 (https://www.iprox.cn)
Lipidomics data	This paper	OMIX: OMIX002016 (https://ngdc.cncb.ac.cn/omix)
Experimental models: Organisms/strains		
Mouse: 6-week-old male C57/BL6 mice	Shanghai SLAC Laboratory Animal Co., Ltd.	N/A
Software and algorithms		
Cytoscape	Shannon et al., 2003	https://cytoscape.org/
flexImaging (version 4.0)	Bruker Daltonics, Billerica, MA, USA	N/A
Firmiana	Feng et al., 2017	https://phenomics.fudan.edu.cn/firmiana/gardener/
Proteome Discover (version 2.3)	Thermo Fisher Scientific, CA, USA	N/A
LipidSearch (version 4.2)	Thermo Fisher Scientific, CA, USA	N/A

RESOURCE AVAILABILITY

Lead contact

Further information and requests for resources and reagents should be directed to and will be fulfilled by the lead contact, Chen Ding (chend@fudan.edu.cn).

Materials availability

All unique/stable reagents generated in this study are available from the lead contact without restriction.

Data and code availability

- The proteomics and phosphoproteomics data have been deposited to the public database iProX: PXD039460 (https://www.iprox.cn). The lipidomic data were deposited to the public database OMIX: OMIX002016 (https://ngdc.cncb.ac.cn/omix). We also supplied the quantitative data matrix and the processed data of proteome, phosphoproteome, and lipidome in our supplementary tables.
- This paper does not report original code.
- Any additional information required to reanalyze the data reported in this paper is available from the lead contact upon request.

EXPERIMENTAL MODEL AND SUBJECT DETAILS

Animals

C57BL/6 mice (male) were ordered from Shanghai SLAC Laboratory Animal Co., Ltd. (Shanghai China) and housed under a standard SPF laboratory environment until they were eight-weeks-old. All animal experiments were approved by the animal care regulations of the Institutional Animal Care and Use Committee of Fudan University. All procedures were approved by IACUC, Fudan University. Ethical review approval number 2018JS0027 was obtained from the Department of experimental animal science, Fudan University.

METHOD DETAILS

H&E staining

Eye tissues were fixed in formalin, embedded in paraffin, cut into 5 μm sections. After deparaffinization and rehydration, 5 μm longitudinal sections were stained with hematoxylin solution for 5 min followed by 5 dips in 1% acid ethanol (1% HCl in 70% ethanol) and then rinsed in distilled water. They were next stained with eosin solution for 3 min followed by dehydration with graded alcohol and cleaning in xylene. The mounted slides were then examined and photographed using an Olympus BX53 fluorescence microscope (Tokyo, Japan).

Stimulated Raman scattering (SRS) microscope and laser microdissection

Our imaging system used SRS, SHG and TPEF microscopy modalities to detect the distribution of lipids and protein, collagen and elastin.[5,6] Their schematic energy diagrams are shown in Figure S1A. SRS is a coherent nonlinear optical version of Raman scattering. When both the pump and Stokes photons interact with the sample with their frequency difference matches with the vibrational frequency of a specific chemical bond in a biomolecule, the Raman process is enhanced by several orders of magnitude.[54–56] SHG occurs when the ultrashort laser pulses interact with non-central symmetric medium and generated photons of the twice the excitation frequency, and is usually sensitive to collagen fibers in biological specimens.[57,58] In TPEF, our 802 nm laser beam excited two-photon autofluorescence from elastin fibers. As a label-free and sensitive imaging modality, multimode microscopy allows mapping of molecular species in sections or fresh tissues with high speed.

The setup of our multimode imaging system is demonstrated in Figure S1B. We used a commercial femtosecond (fs) optical parametric oscillator (OPO, Insight DS+, Newport) with dual outputs as the light source. The fundamental 1040 nm beam (~200 fs) was used as the Stokes, and the wavelength tunable output (690–1300 nm, ~150 fs) was used as the pump. The femtosecond pulses were chirped through high dispersive glass rods (SF57) to several picoseconds (pump: ~3.8 ps, Stokes: ~1.8 ps) to realize spectral focusing to obtain high-resolution spectra. These picosecond lasers were also used as microdissection lasers. The Stokes beam was modulated by an electro optical modulator (EOM) at 10 MHz, and collinearly combined with the pump beam through a dichroic mirror (DMSP1000, Thorlabs). The combined beam was delivered to the laser scanning microscope (FV1200, Olympus) and focused onto the samples with a 20X objective (NA 0.9, Olympus, Japan). The transmitted stimulated Raman loss (SRL) signal of the pump beam was filtered with a band-pass filter (CARS ET890/220, Chroma), detected with a home-built back-biased photodiode and demodulated with a lock-in amplifier (HF2LI, Zurich Instruments) to generate pixel data for the microscope, and form SRS images by laser scanning. In this study, the pump beam was fixed at 802 nm center wavelength, and imaged at Raman frequencies of 2845 cm^{-1} for lipid and 2930 cm^{-1} for protein decomposition following the established linear algorithm.[59] The SHG signal generated by collagen fiber (excited at 804 nm and emitted at 402 nm) was detected using a narrow band-pass filter (FF01-405/10–25, Semrock) with a photomultiplier tube (PMT). Whereas the TPEF signal generated by elastin (emitted at 545 nm–605 nm) was detected by a broad band-pass filter (FF01-575/59-25) and a PMT. All the optical signals were simultaneously detected with SRS in the transmission mode and SHG/TPEF in the epi mode. Each slide was surveyed with the microscopy system in four channels immediately after sectioning.

Each image was scanned with a pixel dwelling time of 2 us, and a size of 512 × 512 pixels. We checked the evenness of each identified area by adjusting the focus quickly before micro-dissection to make sure there was no big morphology change within the 30 μm thick tissue. The detection limit of biomolecules is usually at mM concentration, and the spatial resolution of SRS is ~500 nm. When we decided to dissect the region, the laser power was then increased (240 mW post objective), and scanned along the defined dissection border, and the condenser was switched to centrifuge to collect tissue, as shown in (Figure S1C). During dissection, the laser repeatedly scanned 500 times over the border, and resulting 10 ms dwelling time on each pixel of the border, hence effectively incised the polyethylene napthalate (PEN) membrane from the glass slide, facilitating the cutting and catapulting of ROI (region of interest).

The collection of aqueous humor and vitreous humor

Due to the liquid state and the small size of mouse eye, aqueous humor and vitreous humor were collected by dissection and centrifugation. After the mice were euthanized, the cornea was cut open, then aqueous humor was aspirated by cotton sliver, transferred to a Microcon filtration device, and collected by centrifugation from cotton sliver. After aqueous humor was aspirated, the lens, vitreous humor, and retina were taken out through squeezing the back part of the eye ball by elbow tweezers, and transferred to a Microcon filtration device. Then the liquid of vitreous humor was collected by centrifugation separated from lens and retina.

Protein extraction and tryptic digestion

The proteins of aqueous humor and vitreous humor were collected by acetone precipitation. The required volume of acetone was cooled to −20°C. Protein sample was placed in acetone-compatible tube. four times the sample volume of cold (−20°C) acetone was added to the tube. Vortex tube and incubate for 120 min at −20°C. The crude extract was then clarified via centrifugation at 16,000 × g for 10 min, and the supernatant was loaded into a 10 kD Microcon filtration device (Millipore), centrifuged at 12,000 × g for 20 min, and then washed twice with Urea lysis buffer (8 M Urea, 100 mM Tris-HCl pH 8.0) and twice with 50 mM NH4HCO3. The samples were digested using trypsin overnight at 37°C. The samples of the other 9 regions collected by laser microdissection were minced in Urea lysis buffer (8 M Urea, 100 mM Tris-HCl pH 8.0). The lysate was reduced with 10 mM dithiothreitol (DTT) at 56 °C for 30 min and alkylated with 10 mM iodoacetamide at room temperature in the dark for additional 30 min. About 100 μg of protein samples were loaded into a 10 kD Microcon filtration device (Millipore) and digested using trypsin overnight at 37°C. Finally, the peptides were extracted and dried (SpeedVac, Eppendorf).

First dimensional reversed-phase separation

The dried peptides were loaded into a homemade Durashell Reverse Phase column (2 mg packing [3 μM, 150 Å, Agela] in a 200 μL tip) and then eluted sequentially with nine gradient elution buffers that contained mobile phases A (2% acetonitrile [ACN], adjusted pH to 10.0 using $NH_3.H_2O$) and 6%, 9%, 12%, 15%, 18%, 21%, 25%, 30%, and 35% of mobile phase B (98% ACN, adjusted pH to 10.0 using $NH_3.H_2O$). The nine fractions were then combined into three groups (6% + 15% + 25%, 9% + 18% + 30%, and 12% + 21% + 35%), and dried under vacuum for subsequential MS analysis.

Enrichment of phosphorylated peptides

For the phosphoproteomic analysis, peptides were extracted after trypsin digestion using the methods described above. The tryptic peptides were then enriched with High-Select Fe-NTA Phosphopeptide Enrichment Kit (Thermo Scientific cat. A32992), following the manufacturer's recommendation. Briefly, peptides were suspended with binding/wash buffer (contained in the enrichment kit), mixed with the equilibrated resins, and incubated at 21–25°C for 30 min. After incubation, the resins were washed thrice with binding/wash buffer and twice with water. The enriched peptides were eluted with elution buffer (contained in the enrichment kit), and dried in a SpeedVac.

LC-MS/MS analysis of peptides

LC-MS/MS of peptides were performed on Easy-nLC liquid chromatography system (Thermo Scientific) coupled to an Orbitrap Fusion Lumos Tribrid platform with FAIMS (Thermo Fisher Scientific). The peptides were dissolved with 10 μL loading buffer (5% methanol and 0.2% formic acid), and 5 μL was loaded onto a 360 μm I.D. × 2 cm, C18 trap column at a maximum pressure 280 bar with 12 μL solvent A (0.1% formic acid in water). Peptides were separated on 150 μm I.D. × 15 cm column (C18, 1.9μm, 120 Å, Dr. Maisch GmbH) with a linear 5–35% Mobile Phase B (ACN and 0.1% formic acid) at 600 nL/min for 75 min. FAIMS separations were performed with the following settings: inner electrode temperature = 100°C (except where noted), outer electrode temperature = 100°C, FAIMS carrier gas flow = 2.3 L/min. The dispersion voltage (DV) was set at−5000 V, and the compensation voltage was stepped into 40 V, 55 V and 70 V.

These analyses utilized a 120,000 resolving power survey scan with AGC = 3 000 000, followed by MS/MS of the most intense precursors for 80 ms. The MS/MS analyses were performed by1.6 m/z isolation with the quadrupole, normalized HCD (higher-energy collisional dissociation) collision energy of 27%, and analysis of fragment ions in the ion trap using the "Turbo" speed scanning from 200 to 1200 m/z. Dynamic exclusion was set to 12 s. Monoisotopic precursor selection (MIPS) was set to Peptide, maximum injection time was set to 20 ms, AGC target was set to 20,000, and charge states unknown, +1, or >+5 were excluded and the advanced peak determination was toggled on.

Peptide identification and protein quantification

MS raw files were processed with ''Firmiana'' (a one-stop proteomic cloud platform[60]) against the mouse RefSeq protein database (updated on 04-07-2013) in the National Center for Biotechnology Information. The maximum number of missed cleavages was set to two. A mass tolerance of 20 ppm for precursor and 0.5 Da for production was allowed. The fixed modification was carbamidomethyl (C), and the variable modifications were N-acetylation and oxidation of methionine. For the quality control of protein identification, a target-decoy-based strategy was applied to control the FDR of both the peptides and proteins to less than 1%. Percolator was used to obtain the probability value (q value), and to validate the FDR (measured by the decoy hits) of every peptide-spectrum match (PSM) lower than 1%. Thereafter, all the peptides with lengths shorter than seven amino acids were removed. The cutoff ion score for peptide identification was 20. All PSMs in all fractions were combined for protein quality control, which is a more stringent quality control strategy. The q values of both the target and decoy peptide sequences were dynamically increased until the corresponding protein FDR was less than 1% using the parsimony principle. For the protein abundance calculation, the non-redundant peptide list was used to assemble the proteins by following the parsimony principle. Thereafter, the protein abundance was estimated with a traditional label-free, intensity-based absolute quantification (iBAQ) algorithm, which divided the protein abundance (derived from intensities of the identified peptides) by the number of theoretically observable peptides.[61] The iBAQ algorithm has been used in multiple proteomic studies.[8,62–64] The fraction of total (FOT), a relative quantification value that was defined as a protein's iBAQ divided by the

total iBAQ of all identified proteins in one experiment, was calculated as the normalized abundance of a particular protein in the experiments. Finally, the FOT was further multiplied by 1e6 for the ease of presentation, and NA values were replaced with 1e-5 to adjust extremely small values.

Quantification of phosphopeptides and phosphoproteins

For the phosphoproteomic data, the intensities of the phosphopeptides were extracted from the Proteome Discover (version 2.3). For the phosphoprotein abundance calculation, the non-redundant phosphopeptide list was used to assemble the proteins by following the parsimony principle. Next, the phosphoprotein abundance was estimated by a traditional label-free, iBAQ algorithm, which divided the protein abundance (derived from the intensities of the identified peptides) by the number of theoretically observable peptides.[61] For phosphosite localization, the ptmRS[65] was used to determine phosphosite confidence and phosphosite probability >0.75 is considered as confident phosphosites.

MALDI-TOF imaging

Mouse eye was frozen after extraction with no additional pre-processing. The sample was embedded in carboxymethylcellulose (CMC) and cryosectioned at the sagittal plane at 10 μm thickness. Dihydroxybenzoic acid solution (DHB) was applied as the matrix deposition on the lipids. 15 mg/mL DHB in 90% ACN with 0.1% (v/v) trifluoroacetic acid (TFA) was applied on the sections of mouse eye by standard DHB method with HTX TM Sprayer (Bruker, Germany). α-Cyano-4-hydroxycinnamic acid solution (HCCA) was applied as the matrix deposition on the glycans. 7 mg/mL HCCA in 50% ACN with 0.1% (v/v) trifluoroacetic acid (TFA) was applied by standard post digestion HCCA deposition method with HTX TM Sprayer (Bruker, Germany).

Sections of the mouse eyes were imaged using a Bruker ultrafleXtreme MALDI-TOF/TOF imaging system capable of acquiring spectra at up. Laser power and laser focus position were manually fine-tuned before each acquisition to ensure optimal data quality and comparable signal intensity. Imaging experiments were controlled by the flexImaging 4.0 software (Bruker Daltonics, Billerica, MA, USA) with a laser raster size of 50 μm^2. At each raster position, 700 laser shots were summed to generate a representative spectrum for each pixel for lipids. All spectra of lipids were obtained in the positive ion reflection mode with delayed ion extraction at a scan range of 300−1,400 m/z.

To effectively handle datasets, the SCiLS lab software application was employed. Spatial segmentation was achieved by using a clustering algorithm defining spectra as belonging to a distinct spatial group. To compare lipid abundance data from the whole mouse eye regions, we used a ROC curve approach to evaluate m/z value based on its discriminating power. Area under the curve (AUC) values between 0 and 1 were obtained for each m/z value describing a signal's discriminatory power based on its normalized relative abundance. With an area under the curve (AUC) of $\geq$0.70 being required for a peak was considered as statistically significant.

Lipid extraction

MS water (200 μL) and methanol (240 μL) was added to a sample aliquot, and the tube was vortexed. After grinding beads was added to each tube, the grinding tube was placed in the precooled adapter, the frequency of the grinding instrument was set to be 60Hz, the grinding operation to be 15s, the grinding interruption to be 5s, and the grinding operation times to be 10 min. Then, 800 μL of methyl tert-butyl ether [MTBE] was added, and the mixture was placed in the ultrasonic cleaner for ice bath ultrasonic for 30 min. After the mixture was centrifuged at 14,000 g for 10 min, the upper (organic) phase was collected and dried.

LC-MS/MS analysis of lipids

LC-MS/MS of lipids were performed on Easy-nLC liquid chromatography system (Thermo Scientific) coupled to Q Exactive HFX platform (Thermo Fisher Scientific). A 2.1 μm I.D. × 100 mm column (Waters, Acclaim C30) was balanced with 70% solvent A (10 mM ammonium formate and 60% ACN in water). The lipids were dissolved with 10 μL loading buffer (50% isopropyl alcohol [IPA] and 50% ACN), and 5 μL was loaded onto a 2.1 μm I.D. × 100 mm column (Waters, Acclaim C30) at 0.26 mL/min. Lipids were separated with a linear 30–100% Mobile Phase B (10 mM ammonium formate and 0.1% formic acid, 90% IPA in ACN) for 20 min.

These analyses utilized a 120,000 resolving power survey scan with AGC = 1 000 000, followed by MS/MS of the most intense precursors for 80 ms. The MS/MS analyses were performed by1.5 m/z isolation with the quadrupole, normalized HCD (higher-energy collisional dissociation) collision energy of 20%, 40%, and 60% and analysis of fragment ions in the ion trap scanning from 200 to 2000 m/z. Maximum injection time was set to 20 ms, AGC target was set to 200,000.

Lipid identification and quantification

Lipid profiles were analyzed by LipidSearch 4.2 (Thermo Fisher Scientific, CA, USA), a leading commercial lipidomics software platform.[66] The target database was Q Exactive HFX and the peak detection was recalc isotope. The search options were as follows: parent tolerance, 5 ppm, product tolerance, 8 ppm; m-score threshold, 2; Quan m/z tolerance ±5 ppm; Quan retention time (RT) range ±0.5 min; use of main isomer filter and for the ID quality filter, A-B; adduct ions, H+ and NH4 + for positive ion mode and H− and HCOO− for negative ion mode. Lipid alignments were performed with below parameters: ExpType, LC-MS; Alignment method, Mean; R. T. Tolerance, 2; Calculate unassigned peak area, on; Filter Type, New Filter; Toprank Filter, on; Main Node Filter, Main isomer peaks; m-Score Threshold, 5.0; ID quality filter: A, B, C and D. The results were extracted using LipidSearch 4.1.3 software. Finally, the lipids were manually filtered according to the following rules: (i) The peak areas of lipids with m-Score <10 were

revised to 0; (ii): The peak areas of the lipids with AreaScore < 0.7 were revised to 0; (iii): The peak areas of the lipids with PeakQuality < 0.9 were revised to 0; (iv): The peak areas of the lipids with Occupy < 5 were revised to 0; (v): The peak areas of the lipids with Grade C and D were revised to 0.

Pathway enrichment analysis

Pathway enrichment analysis was performed by DAVID (https://david.ncifcrf.gov/) and ConsensusPathwayDB (http://cpdb.molgen.mpg.de/), and the significance of the pathway enrichment analysis was determined by Fisher's exact test on the basis of KEGG pathways and categorical annotations, including the GO ''biological process'' term and Reactome (https://reactome.org/).

Immunohistochemistry (IHC)

Mouse eye tissue sections of 5 μM thickness were stained in batches in a central laboratory at the Zhongshan Hospital according to standard automated protocols. IHC was performed using the Leica BOND-MAX auto staining system (Roche). Antibody was introduced, followed by detection with a Bond Polymer Refine Detection DS9800 (Bond). Slides were imaged using an OLYMPUS BX43 microscope (OLYMPUS) and processed using a Scanscope (Leica).

Global heatmap

Two-way hierarchical clustering was applied to the global proteomic data of the samples and proteins to identify the global differential protein expression and protein coexpression patterns.[67] Each gene expression value in the global proteomic expression matrix was transformed to a *Z* score across all the samples. For the sample-wise and protein-wise clustering, distance was set as ''Euclidean distance'', and weight method was ''complete''. The z-score-transformed matrix was clustered using the ''pheatmap'' (version 1.0.12) R package.

Gene-disease association analysis

To better understand the association between cardiac genes and diseases, the core gene lists from protein–protein association analysis in each heart region above were put through the DisGeNET database (http://www.disgenet.org/web/DisGeNET/menu/home) for gene-disease association analysis. The associations are all supported by experimental evidence or previous publications. The associations from the DisGeNET are all supported by expert curated repositories, GWAS catalogs, animal models, and the scientific literature.